APL Materials

RESEARCH ARTICLE | JULY 01 2024

Effect of ion irradiation on superconducting thin films

Katja Kohopää ; Alberto Ronzani ; Robab Najafi Jabdaraghi ; Arijit Bera ; Mário Ribeiro ; Dibyendu Hazra; Jorden Senior ; Mika Prunnila ; Joonas Govenius ; Janne S. Lehtinen ; Antti Kemppinen

APL Mater. 12, 071101 (2024)
https://doi.org/10.1063/5.0202851

AIP Publishing

APL Materials ARTICLE pubs.aip.org/aip/apm

Effect of ion irradiation on superconducting thin films

Cite as: APL Mater. 12, 071101 (2024); doi: 10.1063/5.0202851
Submitted: 7 February 2024 • Accepted: 12 June 2024 •
Published Online: 1 July 2024

Katja Kohopää,[1,a)] Alberto Ronzani,[1] Robab Najafi Jabdaraghi,[2] Arijit Bera,[2] Mário Ribeiro,[1] Dibyendu Hazra,[1] Jorden Senior,[1,3] Mika Prunnila,[1] Joonas Govenius,[1] Janne S. Lehtinen,[1] and Antti Kemppinen[1]

AFFILIATIONS

[1] QTF Centre of Excellence, VTT Technical Research Centre of Finland Ltd, P.O. Box 1000, FI-02044 VTT, Finland
[2] VTT Technical Research Centre of Finland Ltd., P.O. Box 1000, FI-02044 VTT, Finland
[3] IST Austria, Am Campus 1, 3400 Klosterneuburg, Austria

[a)] **Author to whom correspondence should be addressed:** katja.kohopaa@vtt.fi

ABSTRACT

We demonstrate ion irradiation by argon or gallium as a wafer-scale post-processing method to increase disorder in superconducting thin films. We study several widely used superconductors, both single-elements and compounds. We show that ion irradiation increases normal-state resistivity in all our films, which is expected to enable tuning their superconducting properties, for example, toward a higher kinetic inductance. We observe an increase in superconducting transition temperature for Al and MoSi and a decrease for Nb, NbN, and TiN. In MoSi, ion irradiation also improves the mixing of the two materials. We demonstrate the fabrication of an amorphous and homogeneous film of MoSi with uniform thickness, which is promising, for example, for superconducting nanowire single-photon detectors.

I. INTRODUCTION

Disorder, manifested by normal-state resistivity, has significant effects on the superconducting properties of thin films, which are of continuing scientific interest.[1–4] Ultimately, superconductivity can be observed in films up to the sheet resistance of $R_\square \sim R_Q = h/(4e^2) \approx 6.5\ \mathrm{k\Omega}$,[5,6] where R_Q is the quantum resistance of Cooper pairs, h is the Planck constant, and e is the elementary charge. Above that, superconductivity is destroyed by fluctuations and a superconductor–insulator transition arising from the localization of Cooper pairs.[6] Below that limit, disordered superconductors are of topical applied interest: For example, high $R_\square$ yields a high sheet kinetic inductance $L_\square \simeq hR_\square/(2\pi^2\Delta)$ in the superconducting state, where Δ is the superconducting energy gap. High $L_\square$ allows compact superinductors for quantum information processing.[7,8] Disorder also enables magnetic field resilient superconductivity,[9] quantum phase slip (QPS) devices for quantum metrology,[10,11] and superconducting nanowire single-photon detectors (SNSPDs) for quantum communication.[12,13] Typical $R_\square$ may span roughly 1–4 kΩ for superinductors or QPS and 100–200 Ω for SNSPDs.

High normal-state resistivity can arise from either the granular or amorphous structure. However, many applications benefit from homogeneous materials where: (i) the grain size is too small to support local superconductivity inside a single grain[14] and (ii) the grain size is smaller than any critical dimensions of the structures made from the material. Nanostructures, in particular, become irreproducible unless the material is either amorphous or has small grains. Improving homogeneity enables uniform films also at small thicknesses, which further enhances $R_\square$ and $L_\square$. In principle, irreproducibility could also be solved with novel, single-crystalline two-dimensional superconductors,[15,16] but their processing currently lacks the maturity required for large-scale fabrication.

In this article, we study the usage of broad-beam ion irradiation by argon or gallium for increasing disorder in superconducting thin films. Our wafer-scale post-processing method is applicable to any material regardless of the film deposition method, but here we focus on sputtering, which typically yields polycrystalline films. Physical collisions of the ions may, for example, cause a dense distribution of lattice defects that scatter electrons or even dismantle grains, thus improving the functional homogeneity of the materi-

als. Since conventional superconductivity arises from the interplay between electrons and lattice, it is expected that such structural manipulation also affects the critical temperature T_c, but the direction of the change is less obvious. This motivates our investigation of processing several superconductors, both the most common single-element materials (Al, Nb) and compounds in two widely used groups: nitrides (TiN, NbN) and silicides (MoSi).

Already since the 1950s, several studies on single-element materials, e.g., Al, W, Ga, and Mo, have demonstrated an increase of T_c when the growth of large grains has been prevented, e.g., by evaporating on a cold substrate or in the presence of oxygen, or by creating a layered structure with other materials.[5,17–21] Evaporating with oxygen is a key fabrication step for modern superinductors based on granular aluminum.[7,8,22] In contrast, decreasing the grain size in sputtered niobium by controlling the deposition parameters yields a significant decrease of T_c;[23] however, proton irradiation has been observed to cause only a slight decrease of T_c in Nb while increasing its upper critical field.[24] Other examples of the subtle interplay between disorder and superconductivity include, for example, a significant decrease of T_c in several high-T_c compounds with an A-15 lattice due to neutron irradiation[25] and the dependence of T_c on the crystalline phase of tungsten.[26]

The disordered structure is unstable in many single-element materials, and already room temperature conditions are sufficient to crystallize them into relatively large grains. Disorder can be stabilized, for example, with oxidized grain surfaces or alloyed compounds, which may already be of interest in terms of increased T_c.[27] One such compound with a metastable disordered phase is MoSi, which is a well-known material for SNSPDs and can be fabricated, for example, by sputtering from an alloy-target to a cooled substrate[28] or by co-sputtering at room temperature.[29,30] In the referred experiments, the optimal stoichiometry was found to be about 80% Mo and 20% Si, as a result of a trade-off between maintaining the stability of an amorphous phase, which requires Si, and maximizing T_c, which would favor electron-dense amorphous Mo. The maximum T_c of MoSi in these experiments was 7.9 K,[30] which is significantly higher than in crystalline Mo_3Si, which has almost the same stoichiometry, but T_c of only 1.3 K.[31] According to Ref. 30, T_c of amorphous co-sputtered MoSi decreases rapidly in Mo-poor MoSi when the fraction of Mo is below 45%. Other methods for fabricating disordered MoSi and other silicides include mixing a deposited metal film into a silicon substrate by ion irradiation[32] or by annealing, a technique that was used in the observation of QPS.[33]

The critical temperature of polycrystalline, moderately disordered ($R_\square \sim 10\ \Omega$ for ~100 nm film) NbN films has been found to be relatively insensitive to ion or neutron irradiation.[34] However, ion irradiation of superconducting nitrides has recently been utilized for the fabrication of various components or devices, e.g., helium irradiation for superconducting nanowires from NbN[35,36] and for highly tunable Josephson junctions from NbTiN.[37] Argon irradiation has also been used for tuning the local critical current density of NbTiN superconductor wide strip photon detectors.[38]

Recently, it has been shown that focused ion beam (FIB) irradiation by gallium or helium ions increases T_c and $R_\square$ of MoSi formed by thermal annealing.[39] However, the FIB method is a relatively slow direct-writing process, with timescale proportional to the processed area. In the present work, we focus on broad beam ion irradiation treatment that allows wafer-scale processing. We perform a more systematic study of MoSi, including structural imaging, and extend this study into several other materials of interest.

II. MATERIALS AND METHODS

Figure 1 illustrates our process and wafer structure and shows the corresponding transmission electron microscope (TEM) image of a (non-ideal) MoSi wafer taken after the ion irradiation treatment. The thin films were sputtered on top of a silicon wafer terminated by a silicon dioxide layer. As the next step, we protected some of the wafers with a dielectric layer, because thin films might be sensitive to aging due to oxidation and wafer-scale processing may require significant shelf life. We experimented two dielectrics: 20 nm SiO_2 grown by plasma enhanced chemical vapor deposition (PECVD) and 15 nm Al_2O_3 grown by atomic layer deposition (ALD). If necessary, both layers can also be later removed by selective etching.

The wafers were irradiated with either argon or gallium ions. As a noble gas, argon may irradiate without any doping of the superconducting film. Meanwhile, the atomic mass of gallium ions yields a closer match for most superconductors, which results in more efficient momentum transfer per impact, and allows smaller ion fluences. Gallium also provided promising results in Ref. 39 without any evidence of doping problems. Due to the inevitably large number of other variables in our study, we kept the ion acceleration voltage *qualitatively* constant for all wafers by choosing values that maximize the fraction of kinetic energy deposited into the superconducting film. For this purpose, we performed Monte Carlo simulations (not shown) to optimize the voltage for each combination of wafer stack and ion. The resulting different *quantitative* acceleration voltages are reported in the supplementary material. Due to this approach, the majority of the irradiation ions are deposited into the film. We report the irradiation fluences in units of $Å^{-2} = 10^{16}\ cm^{-2}$ to provide intuitive into the amount of irradiated ions on the atomic scale.

Table I provides an overview of the thin film materials, their targeted sputtering thicknesses, protective layers, and the ions of the irradiation treatment. For MoSi, we performed a study of the effect of ion fluence for Mo-rich stoichiometry (M-series wafers) and a smaller number of process variants for Si-rich stoichiometry (S-series).

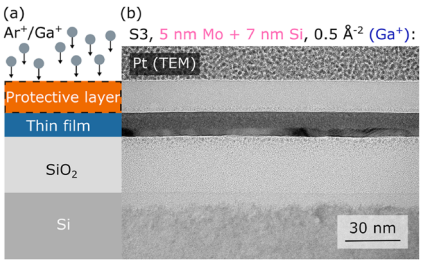

FIG. 1. (a) Illustration of the wafer structure and the ion irradiation process. (b) Transmission electron microscope image of MoSi film S3. The layer of platinum on top of the protective layer was deposited for the TEM imaging and is not a part of the actual fabrication process. The title describes the nominal thicknesses of the sputtered Mo and Si layers as well as the ion fluence.

TABLE I. Overview of thin film materials, their nominal sputtered thicknesses (those of Mo + Si for MoSi), protective layers, and ions for irradiation.

Material	Thickness (nm)	Protective layer	Ion
	Single elements		
Al	14	None	Ar^+
Nb	20	Al_2O_3/none	Ar^+
	Nitrides		
TiN	10	Al_2O_3/none	Ar^+
NbN	10	Al_2O_3/none	Ar^+
	Silicides		
MoSi (M-series)	10 + 7	SiO_2/Al_2O_3	Ar^+/Ga^+
MoSi (S-series)	5 + 7	Al_2O_3	Ar^+/Ga^+
MoSi (S-series)	3 + 7	Al_2O_3	Ar^+/Ga^+

Nitrides were deposited by reactive sputtering of Nb or Ti in a flow of argon and nitrogen. For TiN, we used a recipe that produces $T_c \approx 3$ K. For NbN, the maximum T_c of 14 K is obtained with 1:1 stoichiometry,[40] but in this work, we aimed at high $R_\square$ by utilizing two higher nitrogen flow values. Below, we denote these materials as NbN and NbN*, and their expected values of T_c are 7 and 6 K, respectively.

For MoSi films, first, a layer of molybdenum and then a layer of silicon were deposited, which allowed tuning the targeted stoichiometry by changing the ratio of the film thicknesses. The thickness estimates are based on longer depositions using the same sputtering parameters and measuring the resulting thicker films. However, the short deposition times of thin films increase irreproducibility of their thicknesses. We estimate the stoichiometries of about 65% Mo + 35% Si, 48% Mo + 52% Si, and 35% Mo + 65% Si for our film variants with 10, 5, and 3 nm of Mo (and 7 nm of Si), respectively. The MoSi compounds were formed by annealing in nitrogen environment at 600 °C for 15 min after the deposition of the protective layer. The same temperature (but only for 10 min) was used in Ref. 39 and was expected to yield a compromise between allowing Mo to diffuse into amorphous Si and not allowing Si to crystallize before that, which would prevent forming the compound.[41] However, the optimal annealing of MoSi may depend on many details of the fabrication process, including the thicknesses of the initial Mo and Si layers, and such optimization is beyond the scope of the present work.

In total, we produced 32 irradiated wafers and varied materials, protective layers, and ions and their fluences. We also fabricated reference wafers with the same processes excluding ion irradiation for Al, Nb, TiN, and NbN. We measured $R_\square$ of all wafers at room temperature and imaged most of them with a scanning electron microscope (SEM). We used data from this fast characterization to select an illustrative set of samples for the more elaborate cryogenic characterization (presented in Sec. IV). Based on all these data, a set of seven MoSi films were selected for TEM imaging (Sec. III): identical MoSi films with varied ion fluence, films that seemed visually defective in SEM, MoSi with the highest T_c, and MoSi films that were promising in all the initial measurements.

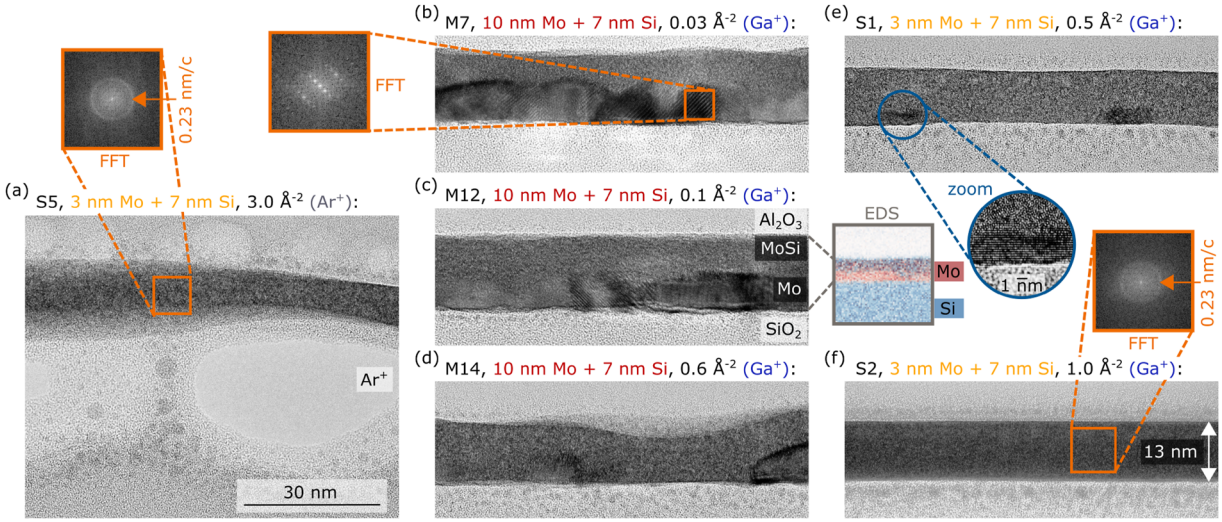

FIG. 2. Transmission electron microscope images of MoSi films S5, M7, M12, M14, S1, and S2 [(a)–(f), respectively]. Images (a)–(f) are on the same scale shown in (a) and (f). The title of each image describes the nominal thicknesses of the sputtered Mo and Si layers and the fluence and ion of the irradiation treatment. The layer stack is the same in each figure: the bright bottom layer is SiO_2 (oxide capping of the silicon wafer) and the bright top layer is of Al_2O_3 deposited to protect the darker layer consisting of Mo and Si. The insets in (a), (b), and (f) show the FFT analysis from the region shown with the orange square. The inset of (c) shows the EDS data of Mo and Si (blue for Si and red for Mo) combined. The gray dashed lines illustrate where the MoSi layer is shown in the EDS inset. The inset in (e) shows the zoom of the region shown with the blue circle.

III. MATERIAL MIXING

Figure 2(a) shows the TEM image of a Mo-poor MoSi film irradiated with argon, which yielded the highest T_c = 5.7 K of all our MoSi films (see Sec. IV). There are gas pockets both in the substrate and in the protective layer, which deform the MoSi film and cause a variation in its thickness. Since the SEM images (not shown) of all argon irradiated MoSi wafers indicated a visually uneven surface, we expect that also they had gas pockets. The energy-dispersive x-ray spectroscopy (EDS) data (not shown) relate the gas pockets to argon. The film is continuous, with grains not resolvable with TEM. Fast Fourier transform (FFT) analysis shows a broad ring at 0.23 nm/cycle. This suggests that the film is amorphous with short-range order corresponding to the nearest neighbor distance.

Figures 2(b)–2(d) show the TEM images of Mo-rich MoSi films treated with an increasing fluence of Ga^+ ions. The films are heterogeneous and have a bilayer structure, with a polycrystalline bottom layer and an amorphous top layer. The inset of the FFT analysis of the bottom layer confirms the crystallinity of the grains. The inset of EDS data indicates that the bottom layer consists mostly of molybdenum, whereas the top layer is a MoSi compound. Higher fluences of gallium reduce the amount of crystalline Mo. Figure 1(b) shows the TEM image of a Mo-poor film (S3) with 5 nm of Mo. The image shows a bilayer structure, similarly as for the Mo-rich films of Figs. 2(b) and 2(c).

Figures 2(e) and 2(f) show the TEM images of Mo-poor MoSi films (S1–S2) with 3 nm of Mo. The thinner layer of molybdenum yields a better intermixing with the silicon top layer; compare Figs. 1(b) and 2(e) with the same gallium fluence of 0.5 $Å^{-2}$. Increasing the fluence to 1.0 $Å^{-2}$ leads to a continuous, homogeneous film of molybdenum and silicon, without TEM-resolvable grains. The FFT analysis shows a broad ring at 0.23 nm/cycle, suggesting that the film is amorphous with short-range order.

Figures 1 and 2 indicate that our annealing process did not result in homogeneous mixing of Mo and Si especially for the Mo-rich stoichiometries, but that ion irradiation improves it. Ion irradiation may thus allow for the fabrication of homogeneous, amorphous MoSi without co-sputtering technology.[28–30] We expect that for a two-layer structure, the mixing improves if the atomic mass of the irradiation ion is closer to that of the top layer rather than to the bottom one. In this respect, Ar^+ (40 u) is more optimal than Ga^+ (70 u) in our case where Si (28 u) is on top of Mo (96 u). Finally, we note that we did not observe significant gas pockets in the TEM images of NbN films (not shown). The present amount of data thus does not rule out the use of Ar^+ ions for irradiation, but it would also be interesting to explore noble gases with higher atomic masses.

An upper limit for the gallium doping of our MoSi films can be obtained by assuming that all ions remain in the superconducting film. For the thinnest film and largest gallium fluence (3 nm Mo + 7 nm Si, 1 $Å^{-2}$), this limit yields the stoichiometry of 30% Mo, 54% Si, and 16% Ga (35% Mo and 65% Si before irradiation).

IV. SHEET RESISTANCE $R_\square$ AND CRITICAL TEMPERATURE T_c

We measured the room temperature sheet resistance $R_{\square,RT}$ with a wafer prober. For cryogenic measurements, we cleaved the wafers into small chips that were fully covered with the film on the top surface. The relative temperature dependence of $R_\square$ down to the base temperature of 0.3 K of our cryostat is recorded through measurements with 4-probe geometry realized by wire bonding. Combining these datasets yields sheet resistance as a function of temperature, $R_\square(T)$.

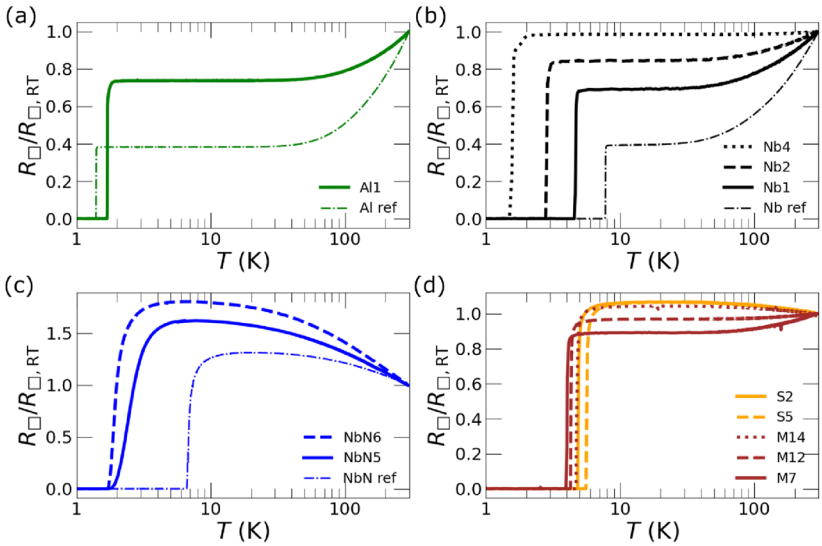

FIG. 3. Normalized sheet resistance $R_\square/R_{\square,RT}$ as a function of temperature for (a) Al, (b) Nb, (c) NbN, and (d) S- and M-series MoSi films. In (a)–(c), "ref" labels reference wafers that were not irradiated.

In this section, Fig. 3 shows the most interesting data on $R_{\square}(T)$ for Al, Nb, NbN, and MoSi. A more comprehensive set of data based on the analysis of all $R_{\square}(T)$ measurements is collated into Table II (see the supplementary material for complete data). Table II also compares irradiated films to values obtained from reference wafers without irradiation. We conclude this section by illustrating the dependencies of Table II in Fig. 4.

The general trend of Fig. 3 is that the residual resistivity ratio (RRR) $R_{\square,\mathrm{RT}}/R_{\square,\mathrm{LT}}$ between room-temperature (RT) and normal-state low-temperature (LT) resistances is higher for the less disordered films (compare to Table II for the resistance values). Panels (a)–(c) show that ion irradiation increases T_c of Al, but decreases those of Nb and NbN. The transitions of NbN, the most disordered of our films, are significantly more smeared than for the others. Figure 3(d) shows that RRR >1 for Mo-rich films, which contain a layer of polycrystalline Mo, and RRR <1 for the better mixed S series films; see Fig. 2. Improving material mixing also increases T_c. A comparison with non-irradiated MoSi wafers is not relevant due to the imperfect mixing of Mo and Si in such films.

Table II shows that ion irradiation and increasing ion fluence increase $R_{\square}$ for all materials. For NbN, there is a significant difference in $R_{\square}$ also between films with and without a protective layer. These results are also illustrated in Fig. 4(a) for Al, Nb, NbN, and TiN.

For MoSi, the interpretation of the results is less straightforward, since most of the films are not homogeneous. The increase in ion fluence reduces the amount of polycrystalline Mo (see Figs. 1 and 2), which we expect to dominate conductivity if there is a continuous layer. In contrast, the T_c measurement of a multilayer stack yields the highest T_c of the stack, but the other layers can still affect the result through the inverse proximity effect. Figure 4(b) illustrates T_c of M- and S-series MoSi as a function of ion fluence. The values of T_c are between 4 and 6 K, and the highest values are obtained for the most disordered Mo-poor films. This result is in ostensible disagreement with Ref. 30, where the highest values of T_c were obtained with Mo-rich films, but our results on Mo-rich films were likely affected by the imperfect mixing. However, our highest T_c for MoSi, 5.7 K (film S5, irradiated with argon), is remarkably high compared to the value 2.8 K obtained for the same stoichiometry in Ref. 30 for co-sputtered, presumably amorphous MoSi.

Figure 4(b) shows one film that had SiO_2 as a protective dielectric (see Table II, wafer M1). All other films in Fig. 4(b) were protected with Al_2O_3. However, several films similar to M1, protected with SiO_2 and irradiated with the same fluence, had repro-

TABLE II. Electrical measurement data for films presented in Fig. 4. The columns describe wafer labels, sputtering deposition thicknesses (Mo + Si for MoSi), protective layers, ions and fluences of the ion irradiation treatments, room temperature sheet resistances before and after ion irradiation treatment, corresponding increases in room temperature sheet resistances, sheet resistances at 10 K, critical temperatures, and the changes in critical temperatures compared to the reference values measured from the wafers without ion irradiation. The ellipses symbol means that the corresponding measurement was not performed. The MoSi films that are shown in Figs. 1 and 2 are indicated in bold.

Label	Dep. thick. (nm)	Prot.	Ion	Fluence ($\mathrm{Å}^{-2}$)	$R_{\square,\mathrm{RT,bef}}$ (Ω)	$R_{\square,\mathrm{RT}}$ (Ω)	$R_{\square,\mathrm{RT}}/R_{\square,\mathrm{RT,bef}}$	$R_{\square,10\mathrm{K}}$ (Ω)	T_c (K)	$T_c/T_{c,\mathrm{ref}}$
Al1	14	None	Ar^+	1.5	2.7	25	9.5	19	1.7	1.2
Nb1	20	None	Ar^+	0.5	13	30	2.3	21	4.7	0.60
Nb2	20	Al_2O_3	Ar^+	0.5	13	40	3.0	33	2.8	0.37
Nb3	20	None	Ar^+	1.5	13	71	5.7	68	1.7	0.22
Nb4	20	Al_2O_3	Ar^+	1.5	13	64	5.0	63	1.6	0.20
NbN3	10	None	Ar^+	1.5	470	2100	4.4	3300	2.6	0.38
NbN5	10	None	Ar^+	1.5	530	3000	5.5	4800	2.6	0.37
NbN6	10	Al_2O_3	Ar^+	1.5	530	1200	2.3	2200	2.0	0.28
NbN7*	10	None	Ar^+	1.5	690	5100	7.3	···	···	···
NbN8*	10	Al_2O_3	Ar^+	1.5	690	1500	2.2	···	···	···
TiN1	10	None	Ar^+	1.5	290	1000	3.7	1200	<0.3	<0.1
TiN2	10	Al_2O_3	Ar^+	1.5	280	640	2.3	720	<0.3	<0.1
M1	10 + 7	SiO_2	Ar^+	1.0	···	120	···	120	4.8	···
M7	10 + 7	Al_2O_3	Ga^+	0.03	···	48	···	43	4.0	···
M11	10 + 7	Al_2O_3	Ga^+	0.06	···	65	···	61	4.0	···
M12	10 + 7	Al_2O_3	Ga^+	0.1	···	71	···	69	4.3	···
M13	10 + 7	Al_2O_3	Ga^+	0.3	···	88	···	90	4.3	···
M14	10 + 7	Al_2O_3	Ga^+	0.6	···	110	···	110	4.8	···
S1	3 + 7	Al_2O_3	Ga^+	0.5	···	170	···	180	5.0	···
S2	3 + 7	Al_2O_3	Ga^+	1.0	···	180	···	190	4.9	···
S3	5 + 7	Al_2O_3	Ga^+	0.5	···	170	···	180	4.1	···
S4	3 + 7	Al_2O_3	Ar^+	3.0	···	140	···	140	5.3	···
S5	3 + 7	Al_2O_3	Ar^+	3.0	···	180	···	190	5.7	···
S6	5 + 7	Al_2O_3	Ar^+	3.0	···	160	···	170	5.5	···

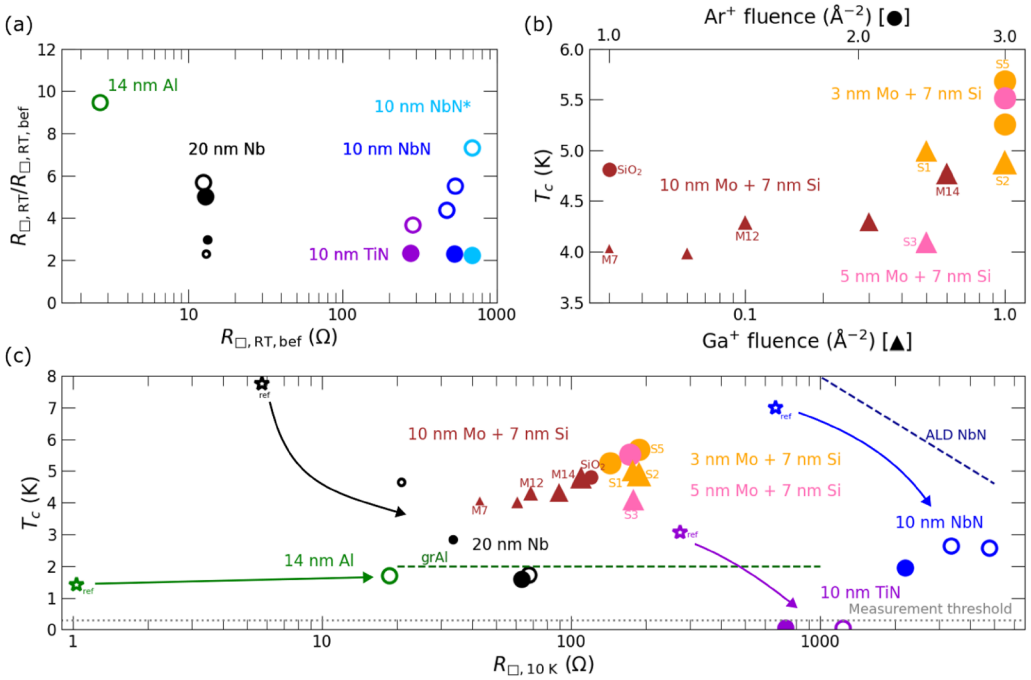

FIG. 4. Relationships between ion fluence, sheet resistance, and superconducting transition temperature measured down to measurement threshold of 0.3 K. The material labels are the nominal thicknesses of the sputtered films, and different colors are used for different materials. The size of the markers illustrates the magnitude of fluence (for argon and gallium independently). The films treated with gallium and argon are shown with triangle and circle markers, respectively. Films that were TEM imaged are labeled. Film that had a SiO_2 protective layer is labeled (other films with a protective layer had Al_2O_3). The empty markers mean that those wafers did not have a protective layer. (a) Increase in sheet resistance due to ion irradiation treatment ($R_{\square,RT}/R_{\square,RT,bef}$) as a function of $R_{\square,RT,bef}$, which is the sheet resistance for otherwise finished wafer but without the ion irradiation treatment. The lighter blue NbN, also marked with asterisk, presents the NbN wafers with higher nitrogen flow (NbN7-8). (b) T_c as a function of argon or gallium ion fluence for M- and S-series of MoSi. (c) T_c as a function of $R_{\square,10K}$. The star markers show (in some cases average) values for wafers that did not undergo ion irradiation treatment, also labeled as "ref." The arrows illustrate the change in parameters due to ion irradiation. Examples of parameter ranges with alternative techniques, granular aluminum (grAl)[42] and ALD-grown NbN,[40] are shown with green dashed and blue dashed lines, respectively.

ducible values of $R_{\square,RT}$ between 98 and 120 Ω; see the supplementary material. The T_c of wafer M1 is also the same as the highest T_c measured from gallium-treated M-series films with the Al_2O_3 layer. Hence, we notice no difference between the two protective layer materials.

Finally, Fig. 4(c) shows the map between T_c and $R_{\square,10K}$ of MoSi, NbN, TiN, Nb, and Al wafers. The reference values of non-irradiated wafers are included for Al, Nb, TiN, and NbN. The increase of T_c in Al and the corresponding decrease in Nb as a function of increased disorder are in qualitative agreement with experiments on granular Al[42] and Nb,[23] but obtained with an entirely different fabrication method. A significantly smaller decrease of T_c, 0.16 K, has been observed in Nb films irradiated with protons,[24] which was in agreement with theoretical calculations.[43] However, the proton-irradiated Nb films had an order of magnitude smaller resistivity than films Nb3–4. A strong decrease of T_c as a function of ion fluence and resistivity makes this elemental material less promising as a disordered superconductor. Meanwhile, lithography-defined irradiation may allow Nb structures of different T_c and $L_\square$ in the same layer.

Ion irradiation yields a significant decrease of T_c for both nitrides. In irradiated TiN, we did not observe superconductivity at and above 0.3 K. The effect of ion irradiation on T_c of our 10 nm NbN films is significantly stronger (~70%) than in thicker and less disordered films studied in Ref. 34 (~10%).

We studied Nb, NbN, and TiN films both with and without protective layers. Our experiments do not indicate any noticeable effect of the protective layer on the measured T_c, but the increase of $R_\square$ was significantly higher for non-protected nitrides. However, this effect may also be attributed to oxidation, i.e., the limited shelf life of thin nitride films.

We consider Fig. 4(c) also as an application-oriented map into disordered superconductors, from which one could pick suitable materials for each purpose. Since ion irradiation is, in principle, suitable for increasing disorder of any superconducting thin film, future research on other materials may help us fill the empty parts of the map. As examples of alternative techniques, tuning the oxidation of granular aluminum provides a wide range of $R_\square$ at $T_c \approx 2$ K,[42] while reducing the thickness of ALD-grown NbN can provide values from about $T_c \approx 14$ K and $R_\square \approx 60$ Ω to $T_c \approx 5$ K and $R_\square \approx 5$ kΩ.[40] These

value ranges of the alternative techniques are illustrated in Fig. 4(c) by the green and blue lines, respectively.

V. DISCUSSION AND CONCLUSIONS

We present a wafer-scale method for increasing disorder in superconducting thin films by using broad beam ion irradiation. Our treatment can be applied independently of the material and its fabrication method, but a permanent effect requires a disordered phase that is stable at room temperature. In contrast to most other techniques, ion irradiation is also expected to allow for limiting the treatment to certain parts of the thin film by lithography, which enables pattern transfer of disorder-induced superconducting properties within the same metallization layer.

We used both gallium and argon ions and studied various single-element (Al and Nb) and compound materials (NbN, TiN, and MoSi). Both ions increased the sheet resistance of the films, but in some cases, argon yielded gas pockets that can be detrimental for applications. As a result of ion irradiation, the critical temperature increased in MoSi and Al, but decreased in TiN, NbN, and Nb.

Both ions were used to produce a MoSi film that is amorphous with some short-range order. We obtained a significantly higher T_c (5.7 K) for the Mo-poor MoSi film (35% Mo, 65% Si) than in the literature (2.8 K).[30] Our Mo-rich MoSi films had the tendency to form a two-layer structure of polycrystalline Mo and amorphous MoSi. Further research on the effect of stoichiometry would benefit from better mixing of the material before ion irradiation, which could be achieved, for example, through co-sputtering from Mo and Si targets or sputtering from a MoSi compound target.

The ion irradiation method enables the tuning of $R_\square$ and T_c of superconducting thin films, potentially expanding the range of promising materials for different devices in quantum technology. In this work, we have demonstrated amorphous and uniform MoSi that is promising for superconducting nanowire single-photon detectors as well as tuning of parameters for Al, Nb, and NbN thin films.

SUPPLEMENTARY MATERIAL

A table that shows information about all wafers of this work is provided in the supplementary material. The first column contains the wafer labels, sputtered materials, protective layers, and sheet resistances in room temperature after deposition. The next column describes the ion irradiation treatment parameters, i.e., ions, fluences, and acceleration voltages. The last column shows the sheet resistances in room temperature after ion irradiation treatment, sheet resistances in 10 K, and critical temperatures. The T_c value is defined as the temperature, where $R(T) = 0.5 \times R_{10K}$. Sheet resistances in room temperature have been measured by a four-point probe in multiple positions of the wafer and the value in the table is the average of those measurements, shown with two significant figures. The asterisk in some NbN wafer labels corresponds to different sputtering parameters; see Sec. II.

ACKNOWLEDGMENTS

We thank J. A. Sauls for useful discussions. For funding of our research project, we acknowledge the European Union's Horizon 2020 Research and Innovation Program under Grant Agreement Nos. 862660/Quantum e-leaps, 899558/aCryComm, 766853/EFINED, and ECSEL programme 101007322/MatQu. This project has also received funding from Business Finland through Quantum Technologies Industrial (QuTI) Project No. 128291 and from Research Council of Finland through Grant Nos. 310909, 350220 and Finnish Quantum Flagship project 359284. This work was performed as part of the Research Council of Finland Centres of Excellence program (Project Nos. 336817, 336819, 352934, and 352935). We also acknowledge funding from an internal strategic innovation project of VTT related to the development of quantum computing technologies. This research was supported by the Scientific Service Units of IST Austria through resources provided by Electron Microscopy Facility. J. Senior acknowledges funding from the European Union's Horizon 2020 Research and Innovation Program under the Marie Skłodowska-Curie Grant Agreement No. 754411. A. Ronzani acknowledges funding from Research Council of Finland (Research Fellowship Project No. 356542).

AUTHOR DECLARATIONS

Conflict of Interest

The authors have no conflicts to disclose.

Author Contributions

All authors read and commented on the manuscript.

Katja Kohopää: Data curation (equal); Formal analysis (equal); Investigation (equal); Visualization (equal); Writing – original draft (equal). **Alberto Ronzani**: Conceptualization (equal); Data curation (equal); Investigation (equal); Visualization (equal); Writing – review & editing (equal). **Robab Najafi Jabdaraghi**: Data curation (equal); Investigation (equal). **Arijit Bera**: Investigation (equal). **Mário Ribeiro**: Formal analysis (equal); Visualization (equal); Writing – review & editing (equal). **Dibyendu Hazra**: Investigation (equal). **Jorden Senior**: Investigation (equal). **Mika Prunnila**: Conceptualization (equal); Funding acquisition (equal). **Joonas Govenius**: Conceptualization (equal); Supervision (equal). **Janne S. Lehtinen**: Conceptualization (equal). **Antti Kemppinen**: Conceptualization (equal); Funding acquisition (equal); Project administration (equal); Supervision (equal); Visualization (equal); Writing – review & editing (equal).

DATA AVAILABILITY

The data that support the findings of this study are openly available in Zenodo at http://doi.org/10.5281/zenodo.12165684.

REFERENCES

[1] P. W. Anderson, "Theory of dirty superconductors," J. Phys. Chem. Solids **11**, 26–30 (1959).

[2] O. V. Astafiev, L. B. Ioffe, S. Kafanov, Y. A. Pashkin, K. Y. Arutyunov, D. Shahar, O. Cohen, and J. S. Tsai, "Coherent quantum phase slip," Nature **484**, 355–358 (2012).

[3] A. Weitzel, L. Pfaffinger, I. Maccari, K. Kronfeldner, T. Huber, L. Fuchs, J. Mallord, S. Linzen, E. Il'ichev, N. Paradiso, and C. Strunk, "Sharpness of the

Berezinskii-Kosterlitz-Thouless transition in disordered NbN films," Phys. Rev. Lett. **131**, 186002 (2023).
[4]M. Mondal, A. Kamlapure, M. Chand, G. Saraswat, S. Kumar, J. Jesudasan, L. Benfatto, V. Tripathi, and P. Raychaudhuri, "Phase fluctuations in a strongly disordered s-wave NbN superconductor close to the metal-insulator transition," Phys. Rev. Lett. **106**, 047001 (2011).
[5]H. M. Jaeger, D. B. Haviland, A. M. Goldman, and B. G. Orr, "Threshold for superconductivity in ultrathin amorphous gallium films," Phys. Rev. B **34**, 4920–4923 (1986).
[6]B. Sacépé, T. Dubouchet, C. Chapelier, M. Sanquer, M. Ovadia, D. Shahar, M. Feigel'man, and L. Ioffe, "Localization of preformed Cooper pairs in disordered superconductors," Nat. Phys. **7**, 239–244 (2011).
[7]N. Maleeva, L. Grünhaupt, T. Klein, F. Levy-Bertrand, O. Dupre, M. Calvo, F. Valenti, P. Winkel, F. Friedrich, W. Wernsdorfer, A. V. Ustinov, H. Rotzinger, A. Monfardini, M. V. Fistul, and I. M. Pop, "Circuit quantum electrodynamics of granular aluminum resonators," Nat. Commun. **9**, 3889 (2018).
[8]L. Grünhaupt, M. Spiecker, D. Gusenkova, N. Maleeva, S. T. Skacel, I. Takmakov, F. Valenti, P. Winkel, H. Rotzinger, W. Wernsdorfer, A. V. Ustinov, and I. M. Pop, "Granular aluminium as a superconducting material for high-impedance quantum circuits," Nat. Mater. **18**, 816–819 (2019).
[9]N. Samkharadze, A. Bruno, P. Scarlino, G. Zheng, D. DiVincenzo, L. DiCarlo, and L. Vandersypen, "High-kinetic-inductance superconducting nanowire resonators for circuit QED in a magnetic field," Phys. Rev. Appl. **5**, 044004 (2016).
[10]J. S. Lehtinen, K. Zakharov, and K. Y. Arutyunov, "Coulomb blockade and bloch oscillations in superconducting Ti nanowires," Phys. Rev. Lett. **109**, 187001 (2012).
[11]R. S. Shaikhaidarov, K. H. Kim, J. W. Dunstan, I. V. Antonov, S. Linzen, M. Ziegler, D. S. Golubev, V. N. Antonov, E. V. Il'ichev, and O. V. Astafiev, "Quantized current steps due to the a.c. coherent quantum phase-slip effect," Nature **608**, 45–49 (2022).
[12]G. N. Gol'tsman, O. Okunev, G. Chulkova, A. Lipatov, A. Semenov, K. Smirnov, B. Voronov, A. Dzardanov, C. Williams, and R. Sobolewski, "Picosecond superconducting single-photon optical detector," Appl. Phys. Lett. **79**, 705–707 (2001).
[13]I. Esmaeil Zadeh, J. Chang, J. W. N. Los, S. Gyger, A. W. Elshaari, S. Steinhauer, S. N. Dorenbos, and V. Zwiller, "Superconducting nanowire single-photon detectors: A perspective on evolution, state-of-the-art, future developments, and applications," Appl. Phys. Lett. **118**, 190502 (2021).
[14]V. F. Gantmakher and V. T. Dolgopolov, "Superconductor–insulator quantum phase transition," Phys.-Usp. **53**, 1 (2010).
[15]Y.-C. Zou, Z.-G. Chen, E. Zhang, F. Xiu, S. Matsumura, L. Yang, M. Hong, and J. Zou, "Superconductivity and magnetotransport of single-crystalline $NbSe_2$ nanoplates grown by chemical vapour deposition," Nanoscale **9**, 16591–16595 (2017).
[16]Y. Cao, V. Fatemi, S. Fang, K. Watanabe, T. Taniguchi, E. Kaxiras, and P. Jarillo-Herrero, "Unconventional superconductivity in magic-angle graphene superlattices," Nature **556**, 43–50 (2018).
[17]W. Buckel and R. Hilsch, "Einfluß der Kondensation bei tiefen Temperaturen auf den elektrischen Widerstand und die Supraleitung für verschiedene Metalle," Z. Phys. **138**, 109–120 (1954).
[18]O. F. Kammerer and M. Strongin, "Superconductivity in tungsten films," Phys. Lett. **17**, 224–225 (1965).
[19]B. Abeles, R. W. Cohen, and G. W. Cullen, "Enhancement of superconductivity in metal films," Phys. Rev. Lett. **17**, 632–634 (1966).
[20]M. Strongin, O. F. Kammerer, D. H. Douglass, and M. H. Cohen, "Effect of dielectric and high-resistivity barriers on the superconducting transition temperature of thin films," Phys. Rev. Lett. **19**, 121–125 (1967).
[21]R. B. Pettit and J. Silcox, "Film structure and enhanced superconductivity in evaporated aluminum films," Phys. Rev. B **13**, 2865–2872 (1976).
[22]L. Grünhaupt, *Granular Aluminium Superinductors* (KIT Scientific Publishing, 2019).
[23]S. Bose, P. Raychaudhuri, R. Banerjee, P. Vasa, and P. Ayyub, "Mechanism of the size dependence of the superconducting transition of nanostructured Nb," Phys. Rev. Lett. **95**, 147003 (2005).
[24]M. A. Tanatar, D. Torsello, K. R. Joshi, S. Ghimire, C. J. Kopas, J. Marshall, J. Y. Mutus, G. Ghigo, M. Zarea, J. A. Sauls, and R. Prozorov, "Anisotropic superconductivity of niobium based on its response to nonmagnetic disorder," Phys. Rev. B **106**, 224511 (2022).
[25]A. R. Sweedler, D. G. Schweitzer, and G. W. Webb, "Atomic ordering and superconductivity in high-T_c A − 15 compounds," Phys. Rev. Lett. **33**, 168–172 (1974).
[26]A. E. Lita, D. Rosenberg, S. Nam, A. J. Miller, D. Balzar, L. M. Kaatz, and R. E. Schwall, "Tuning of tungsten thin film superconducting transition temperature for fabrication of photon number resolving detectors," IEEE Trans. Appl. Supercond. **15**, 3528–3531 (2005).
[27]M. S. Osofsky, R. J. Soulen, J. H. Claassen, G. Trotter, H. Kim, and J. S. Horwitz, "New insight into enhanced superconductivity in metals near the metal-insulator transition," Phys. Rev. Lett. **87**, 197004 (2001).
[28]D. Bosworth, S.-L. Sahonta, R. H. Hadfield, and Z. H. Barber, "Amorphous molybdenum silicon superconducting thin films," AIP Adv. **5**, 087106 (2015).
[29]A. Banerjee, L. J. Baker, A. Doye, M. Nord, R. M. Heath, K. Erotokritou, D. Bosworth, Z. H. Barber, I. MacLaren, and R. H. Hadfield, "Characterisation of amorphous molybdenum silicide (MoSi) superconducting thin films and nanowires," Supercond. Sci. Technol. **30**, 084010 (2017).
[30]X. Zhang, I. Charaev, H. Liu, T. X. Zhou, D. Zhu, K. K. Berggren, and A. Schilling, "Physical properties of amorphous molybdenum silicide films for single-photon detectors," Supercond. Sci. Technol. **34**, 095003 (2021).
[31]H. M. Tütüncü, S. Bağcı, and G. P. Srivastava, "Electronic structure, phonons, and electron-phonon interaction in Mo_3Si," Phys. Rev. B **82**, 214510 (2010).
[32]B. Y. Tsaur, Z. L. Liau, and J. W. Mayer, "Ion-beam-induced silicide formation," Appl. Phys. Lett. **34**, 168–170 (1979).
[33]J. S. Lehtinen, A. Kemppinen, E. Mykkänen, M. Prunnila, and A. J. Manninen, "Superconducting MoSi nanowires," Supercond. Sci. Technol. **31**, 015002 (2017).
[34]J. Y. Juang, D. A. Rudman, J. Talvacchio, and R. B. Van Dover, "Effects of ion irradiation on the normal state and superconducting properties of NbN thin films," Phys. Rev. B **38**, 2354–2361 (1988).
[35]G. D. Martinez, D. Buckley, I. Charaev, A. Dane, D. E. Dow, and K. K. Berggren, "Superconducting nanowire fabrication on niobium nitride using helium ion irradiation," arXiv:2003.02898 (2020).
[36]W. Zhang, Q. Jia, L. You, X. Ou, H. Huang, L. Zhang, H. Li, Z. Wang, and X. Xie, "Saturating intrinsic detection efficiency of superconducting nanowire single-photon detectors via defect engineering," Phys. Rev. Appl. **12**, 044040 (2019).
[37]A. Ruhtinas and I. J. Maasilta, "Highly tunable NbTiN Josephson junctions fabricated with focused helium ion beam," arXiv:2303.17348 (2023).
[38]M. Yabuno, F. China, H. Terai, and S. Miki, "Superconducting wide strip photon detector with high critical current bank structure," Opt. Quantum **1**, 26–34 (2023).
[39]E. Mykkänen, A. Bera, J. S. Lehtinen, A. Ronzani, K. Kohopää, T. Hönigl-Decrinis, R. Shaikhaidarov, S. E. de Graaf, J. Govenius, and M. Prunnila, "Enhancement of superconductivity by amorphizing molybdenum silicide films using a focused ion beam," Nanomaterials **10**, 950 (2020).
[40]S. Linzen, M. Ziegler, O. V. Astafiev, M. Schmelz, U. Hübner, M. Diegel, E. Il'ichev, and H.-G. Meyer, "Structural and electrical properties of ultrathin niobium nitride films grown by atomic layer deposition," Supercond. Sci. Technol. **30**, 035010 (2017).
[41]J. M. Liang and L. J. Chen, "Interfacial reactions and thermal stability of ultrahigh vacuum deposited multilayered Mo/Si structures," J. Appl. Phys. **79**, 4072–4077 (1996).
[42]F. Levy-Bertrand, T. Klein, T. Grenet, O. Dupré, A. Benoît, A. Bideaud, O. Bourrion, M. Calvo, A. Catalano, A. Gomez, J. Goupy, L. Grünhaupt, U. v. Luepke, N. Maleeva, F. Valenti, I. M. Pop, and A. Monfardini, "Electrodynamics of granular aluminum from superconductor to insulator: Observation of collective superconducting modes," Phys. Rev. B **99**, 094506 (2019).
[43]M. Zarea, H. Ueki, and J. A. Sauls, "Effects of anisotropy and disorder on the superconducting properties of niobium," Front. Phys. **11**, 1269872 (2023).